Thermal spin crossover behaviour of two-dimensional Hofmann-type coordination polymers incorporating photoactive ligands

Florence Ragon, Korcan Yaksi, Natasha F. Sciortino, Guillaume Chastanet, Jean-Francois Létard, Deanna M. D'alessandro, Cameron J. Kepert, Suzanne M. Neville

CSIRO PUBLISHING

RESEARCH FRONT

Aust. J. Chem. **2014**, *67*, 1563–1573
http://dx.doi.org/10.1071/CH14188

Full Paper

Thermal Spin Crossover Behaviour of Two-Dimensional Hofmann-Type Coordination Polymers Incorporating Photoactive Ligands

Florence Ragon,[A] *Korcan Yaksi,*[A] *Natasha F. Sciortino,*[A] *Guillaume Chastanet,*[B] *Jean-François Létard,*[B] *Deanna M. D'Alessandro,*[A] *Cameron J. Kepert,*[A] *and Suzanne M. Neville*[A,C]

[A]School of Chemistry, The University of Sydney, Sydney, NSW 2006, Australia.
[B]CNRS, Université de Bordeaux, ICMCB, UPR 9048, F-33600 Pessac, France.
[C]Corresponding author. Email: suzanne.neville@sydney.edu.au

Two spin crossover (SCO)-active 2D Hofmann-type framework materials, $[Fe(3\text{-}PAP)_2Pd(CN)_4]$ (**A**) and $[Fe(4\text{-}PAP)_2Pd(CN)_4]$ (**B**) containing the photoactive azo-benzene-type ligands 3-phenylazo-pyridine (3-PAP) and 4-phenylazo-pyridine (4-PAP) were prepared. These materials form non-porous Hofmann-type structures whereby 2D $[Fe^{II}Pd(CN)_4]$ grids are separated by 3- or 4-PAP ligands. The iron(II) sites of both materials (**A** and **B**) undergo abrupt and hysteretic spin transitions with characteristic transition temperatures $T_{1/2}\downarrow,\uparrow$: 178, 190 K ($\Delta T$: 12 K) and $T_{1/2}\downarrow,\uparrow$: 233, 250 K ($\Delta T$: 17 K), respectively. Photo-magnetic characterisations reveal light-induced excited spin state trapping (LIESST) activity in both **A** and **B** with characteristic T(LIESST) values of 45 and 40 K. Although both free ligands show *trans*- to-*cis* isomerisation in solution under UV-irradiation, as evidenced via absorption spectroscopy, such photo-activity was not observed in the ligands or complexes **A** and **B** in the solid state. Structural analysis of a further non-SCO active isomer to **B**, $[Fe(4\text{-}PAP)_2Pd(CN)_4]\cdot 1/2(4\text{-}PAP)$ (**B·(4-PAP)**), which contains free ligand in the pore space is reported.

Introduction

Functional materials that act as molecular switches, i.e. materials that can undergo reversible changes between different molecular states by application of external stimuli, are promising systems for advanced technologies with possible applications in molecular electronics, data storage, and displays.[1–5] In particular, such materials that show bi-stability at ambient temperatures and pressures are highly sought after. A subclass of magnetic molecular switching materials that display spin crossover (SCO) show considerable promise, because the reversible high spin (HS, $S = 2$ for iron(II)) to low spin (LS, $S = 0$ for iron(II)) transition can occur at room temperature in selected examples.[1,3,4,6] These materials can switch spin state in response to a variety of external stimuli, such as temperature, pressure, light irradiation, and guest molecules, providing a broad scope of opportunities for exploitation.[6,7] In particular, the use of light irradiation to control the switching of SCO materials is an attractive approach because it provides a readily accessible and inexpensive means of providing an external perturbation.[5,8] Two major strategies have thus far been applied to achieving photo-switchable SCO, namely, via the light-induced excited spin state trapping (LIESST) effect and ligand-driven light-induced spin change (LD-LISC). The LIESST effect relies on converting a LS state into a metastable HS state at sufficiently low temperatures (<50 K) using green light irradiation.[9,10] Indeed, though there are a large number of SCO complexes that have been shown to display the LIESST effect, and there are many studies dedicated to understanding the LIESST process,[11–14] the drawback of this phenomenon is that the metastable HS-to-LS relaxation process occurs at relatively low temperatures.[15,16] However, it has been shown that pulsed laser irradiation within a hysteresis loop can result in a photo-thermal effect at room temperature.[17] The alternate approach of LD-LISC is based on incorporating photoactive organic moieties into SCO complexes and exploiting the dramatic electronic and structural consequences of photo-irradiation to change the ligand field and therefore the spin state of the metal ion, leading to molecular switches at ambient temperatures.[18] This approach has been mildly successful; however, there are a few reports of such systems.[19–22] A drawback of this approach is that many of the photo-isomerisation processes under investigation are more efficient in the solution state than in the solid state owing to steric restrictions,[23–25] and the cooperativity of the SCO process is depleted in solution.[3,6]

Recent studies have shown that porous materials, such as metal-organic frameworks (MOFs), provide a suitable platform for photo-active ligand isomerisation to occur in the solid state, as stable crystalline void volumes provide an effective solution-state environment.[26–30] For example, an azo-benzene-functionalised bridging carboxylate ligand was used in the

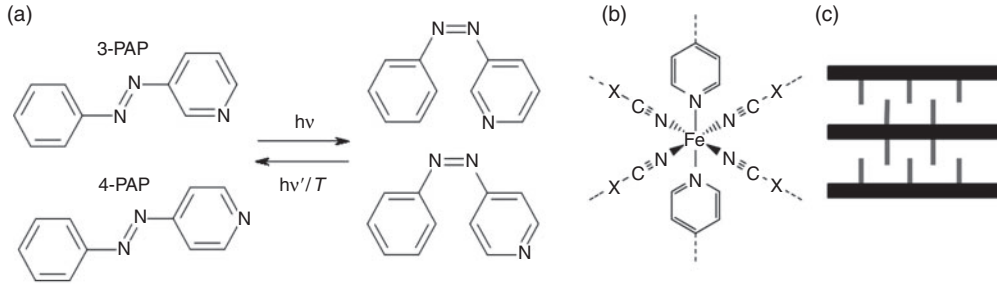

Fig. 1. (a) Ligands 3-PAP and 4-PAP and their *trans* ↔ *cis* photoactive behaviour. (b) Coordination environment of $[Fe^{II}(Pd(CN)_4)(pyridyl)_{2/n}]$. (c) Schematic representation of a 2D layered Hofmann-type framework material.

material PCN-123, whereby the appended photoactive azo-benzene moiety protrudes into the pore cavity.[27] A *trans*-to-*cis* isomerisation process was shown to occur within the pore cavity, leading to controlled uptake and release of guest molecules. Furthermore, the pore cavity of porous MOFs has been shown to be an effective environment to induce solid state isomerisation of embedded photo-active guest molecules.[29]

There are two families of porous framework materials that show dramatic guest sensitive SCO behaviours upon guest removal and exchange. The first group includes SCO framework materials (SCOF-*n*) based on octahedral $[Fe^{II}(NCS)_2(py)_4]$ nodes that are linked to grid-type 2D topologies via bridging organic ligands.[31–36] The porosity in these materials is generated via either the interlacing or stacking of 2D grids. The second family includes SCO Hofmann-type 2- and 3D materials of the type $[Fe^{II}(L)_{2/n}M^{II}(CN)_4]$ (M^{II} = Pt, Pd, Ni, $n = 2$, 1 for bridging or terminal ligands, respectively, Fig. 1b, c) where parallel stacked bimetallic $[Fe^{II}M^{II}(CN)_4]$ layers are linked or separated via organic moieties.[37–44] The porosity in these materials is imparted by the pillared-layered-type topology. Both classes of materials have shown remarkable magnetic variability to guest inclusion, and their SCO character can often be tuned via strategic inter- and intramolecular interactions. Our strategy here is to incorporate a photoactive azo-benzene-type linker into a 2D Hofmann-type SCO material and exploit any pore volume generated to access the *trans*-to-*cis* isomerisation process (Fig. 1a) in the solid state.[26–28] Furthermore, we seek to couple this behaviour with potentially dramatic switching effects on SCO properties.[45] Herein, we focus on 2D systems to harness the flexible nature of the layered structure to further promote such solid state effects.[46,47]

Results and Discussion

Synthesis and Characterisation

Red square plate-like crystals of $[Fe(3\text{-}PAP)_2Pd(CN)_4]$ (**A**) were prepared via slow diffusion techniques, and the composition and purity were determined using single crystal X-ray diffraction, powder X-ray diffraction, thermogravimetric analysis, and elemental analysis (CHN). Similar syntheses involving the 4-PAP ligand led to the formation of a two-phase mixture, consisting predominantly of polycrystalline $[Fe(4\text{-}PAP)_2Pd(CN)_4]$ (**B**) with a small proportion of red square plate crystals of $[Fe(4\text{-}PAP)_2Pd(CN)_4]\cdot 1/2(4\text{-}PAP)$ (**B·(4-PAP)**). The composition of **B** was confirmed by powder X-ray diffraction, thermogravimetric analysis and elemental analyses (CHN) using a sample that had only a minute fraction of **B·(4-PAP)** present. The composition of **B·(4-PAP)** was confirmed by single crystal X-ray diffraction analysis. Attempts to synthesise phase-pure samples by varying the ratio of reactants were unsuccessful. Thermogravimetric analysis of **A** indicated no weight loss up to 500 K, as consistent with the absence of pore solvent (see Fig. S1, Supplementary Material). Thermogram of **B** showed a weight loss of 1.5 % by 400 K, corresponding to either the loss of 0.5 water molecules per iron(II) or the loss of free ligand from the minor **B·(4-PAP)** phase component (Fig. S1). The infrared (IR) spectra of **A** and **B** primarily show the strong stretching vibrational mode of the cyanido groups around 2100 cm^{-1}, consistent with the formation of $[Fe^{II}Pd(CN)_4]$ grids. The powder X-ray diffraction pattern of **A** collected at 200 K is consistent with the simulated pattern generated from single crystal structural data (Fig. S2), and Le Bail refinement confirmed the phase purity of the bulk polycrystalline sample. Powder X-ray diffraction data collected on **B** were indexed to a cell similar to **A** (see discussion below), and confirmed a ~5 % content of **B·(4-PAP)** (pattern simulated from single crystal data).

*Structural Elucidation of **A**, **B** and **B·(4-PAP)***

Single crystal X-ray diffraction data were collected on **A** at 150 and 220 K, and on **B·(4-PAP)** at 100 K. The single crystal structural refinement parameters and structural details are summarised in Table 1, and selected bond lengths, angles, and additional parameters are listed in Table 2. Structural information for **B** was obtained by unit cell analysis of powder X-ray diffraction data.

*Single Crystal Structural Analysis of $[Fe(3\text{-}PAP)_2Pd(CN)_4]$ (**A**)*

Structural analyses were carried out on complex **A** at 150 and 220 K, revealing triclinic symmetry in *P*-1 at both temperatures. The analyses revealed an asymmetric unit consisting of an iron(II) site and $[Pd(CN)_4]^{2-}$ group (both semi occupied owing to their centring on special positions), and a fully occupied 3-PAP ligand (Fig. 2a). The iron(II) centres are in a distorted octahedral environment comprising four equatorially coordinated $[Pd(CN)_4]^{2-}$ metalloligands bound through the N-atoms, and two axially coordinated N-donor monodentate 3-PAP ligands. The equatorial coordination is thus extended to 2D $[Fe^{II}Pd(CN)_4]$ layers which undulate in the *ab*-plane (Fig. 3a, b). The undulating nature of the layer is highlighted by the relative tilt angle of the iron(II) octahedron out of the plane and the deviation of the Fe–N≡C angle from 180°, as summarised in Table 2. The layers are separated by the 3-PAP ligands and in general adopt a 2D interdigitated Hofmann-type topology (Fig. 3c, d). The 3-PAP ligand is approximately planar with respect to the pyridyl- and benzyl-ring orientation, and the 3-coordination mode of the pyridyl group to the iron(II) sites results in a diagonal angle of approach of the 3-PAP ligands into

Table 1. Single crystal structure and refinement details for A and B·(4-PAP)

	$[Fe(3\text{-}PAP)_2Pd(CN)_4]$ (**A**)		$[Fe(4\text{-}PAP)_2Pd(CN)_4]\cdot 1/2(4\text{-}PAP)$ (**B·(4-PAP)**)
Temperature [K]	150	220	100
Formula	$C_{26}H_{18}FeN_{10}Pd$	$C_{26}H_{18}FeN_{10}Pd$	$C_{63}H_{45}Fe_2N_{23}Pd_2$
Formula weight [g mol^{-1}]	632.75	632.75	1448.72
Crystal system	Triclinic	Triclinic	Monoclinic
Space group	*P*-1	*P*-1	$P2_1/c$
a [Å]	6.9698(5)	7.1179(5)	7.3788(2)
b [Å]	7.2924(5)	7.5699(5)	27.9610(7)
c [Å]	12.8763(9)	12.7816(9)	14.8286(4)
α [°]	102.409(5)	100.687(4)	90
β [°]	101.076(5)	99.525(4)	90.017(2)
γ [°]	89.887(4)	90.220(4)	90
V [Å^3]	626.73(8)	667.00(8)	3059.42(14)
D_c [Mg m^{-3}]	1.676	1.575	1.573
Data/restraints/parameters	4402/0/211	5463/0/175	6285/0/406
$R(F)$ ($I > \sigma(I)$, all)	0.0326, 0.0811	0.0368, 0.0855	0.0231, 0.0579
$R_w(F^2)$ ($I > 2\sigma(I)$, all)	0.0432, 0.0957	0.0541, 0.1070	0.0255, 0.0589
GoF	1.087	1.089	1.106

Table 2. Selected single crystal structural parameters of A in the LS and HS states, and corresponding parameters for B·(4-PAP) (HS)

	$Fe(3\text{-}PAP)_2Pd(CN)_4$ (**A**)		$[Fe(4\text{-}PAP)_2Pd(CN)_4]\cdot 1/2(4\text{-}PAP)$ (**B·(4-PAP)**)
Temperature [K]	150	200	100
Fe^{II} spin state	LS	HS	HS
$\sum$ [°][A]	16.8	8.6	19.4
$<d_{Fe-N}>$ [Å][B]	1.96	2.16	2.176
Fe–N≡C [°]	169.8, 170.3	164.7, 161.1	174.81–164.61
Fe–N(C)$_4$ tilt [°][C]	11.99	16.15	15.05
N···C(H) [Å]	3.931(2), 3.946(2)	4.414(5), 4.096(4)	4.242(2)
π–π Interactions [Å]	3.685	3.780	3.738, 3.770

[A]Octahedral distortion parameter calculated by sum of $|90–\theta|$ for the 12 *cis*-N–Fe–N angles in the octahedron.[2]
[B]Average Fe–N distance.
[C]Equatorial out-of-plane octahedral tilt angle.

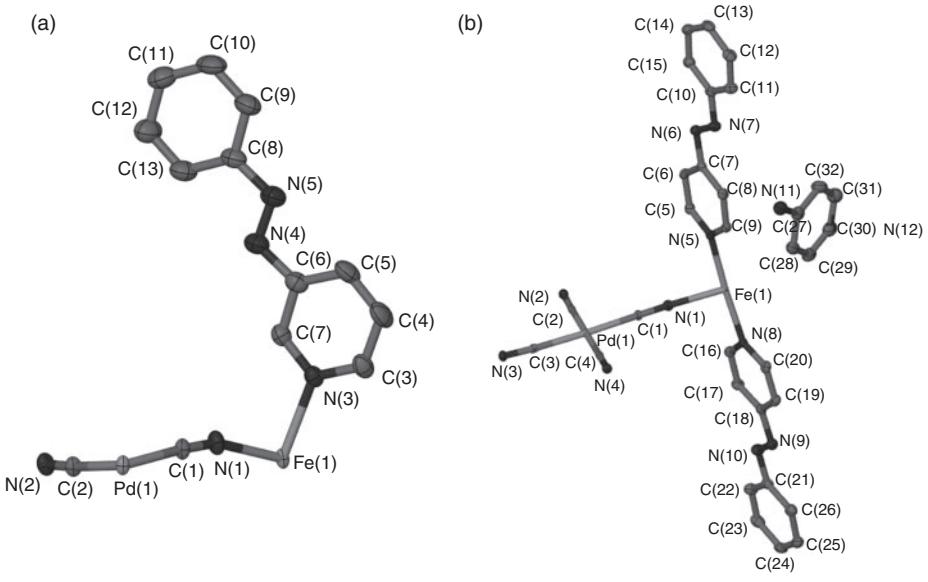

Fig. 2. Asymmetric unit thermal ellipsoid (50 % probability) representation of (a) **A** at 220 K and (b) **B·(4-PAP)** at 100 K. Hydrogen atoms have been omitted.

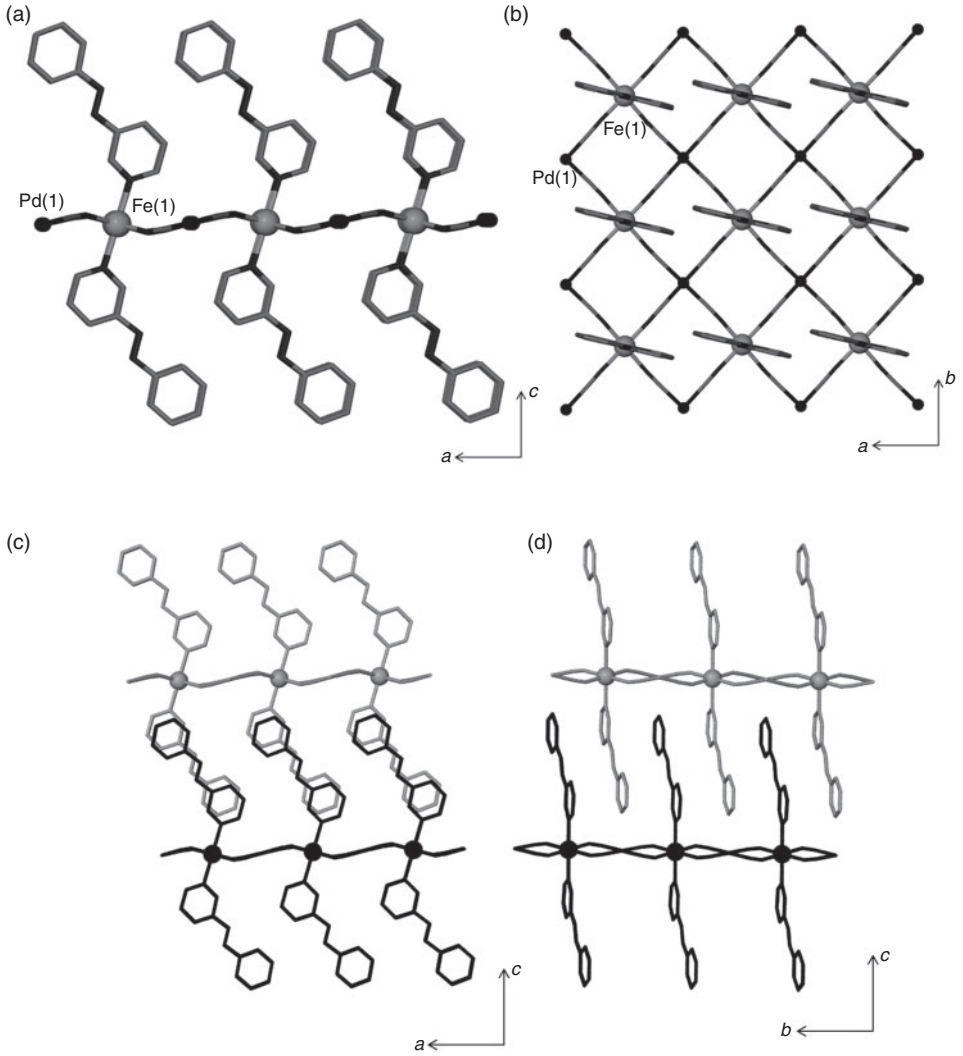

Fig. 3. Structural diagrams of **A** at 220 K: (a) single 2D grid viewed along the *b*-axis and (b) in the *ab*-plane, and two interdigitated layers (grey and black) viewed along the (c) *b*-axis and (d) *a*-axes.

the interlayer spacing (Fig. 3). Adjacent 3-PAP ligands along the *a*-axis within one layer interact via weak N···C(H) interactions between the azo- and benzene groups, respectively (Fig. S7 in the Supplementary Material, Table 2). Adjacent 2D nets are close packed with a near-complete overlap of the interdigitated ligands along the *b*-axis direction (Fig. 3c, d). The 3-PAP ligands stack along the *b*-axis via weak π–π interactions (Fig. 3d, Table 2).

The average Fe–N bond lengths ($<d_{Fe-N}>$, Table 2) at 150 and 220 K of ~1.9 and 2.1 Å confirm that the iron(II) centres are in the LS and HS states, respectively, with the expected 0.2 Å increase from the LS-to-HS states. On the other hand, the octahedral distortion parameter (Σ) increases significantly upon transition from the HS to LS states that is contrary to that expected of the LS state that favours a more regular octahedron (Table 2). Such an inverse behaviour of octahedral distortion has been noted previously in relation to negative-cooperativity, and is generally related to an interplay between inner (i.e. bond length variation) and outer (intra- and intermolecular interactions) coordination sphere effects.[2,48–50] Indeed, here, in assessing the weak hydrogen bonding interactions between adjacent ligands, there is a significant contraction on cooling from the HS to LS states (~0.5 Å), which could account for this behaviour.

Variable temperature powder X-ray diffraction analysis was also carried out on **A** (240–140 K) to assess the overall structural changes over a broad temperature range. These data revealed a single-phase behaviour over the entire SCO temperature range, detailing pronounced, abrupt shifts in Bragg reflections associated with the reversible HS-to-LS transition (Fig. 4a). Le Bail analysis of individual patterns revealed a unit cell evolution that mimics the abrupt and hysteretic magnetic switching behaviour as discussed below (Fig. 4b).

*Structural Analysis of [Fe(4-PAP)$_2$Pd(CN)$_4$] (**B**)*

Variable temperature powder X-ray diffraction data were collected on **B** over the range of 280–200–280 K. Representative plots are shown in Fig. 5 at 290 and 220 K for the HS and LS states, respectively. Unit cell analysis of the 280 K data revealed a triclinic cell (*P*-1) with unit cell dimensions $a = 6.93$, $b = 7.59$, $c = 14.13$ Å, $\alpha = 108.65°$, $\beta = 97.80°$, $\gamma = 90.12°$, $V = 697$ Å^3.[51] The unit cell *a*- and *b*-dimensions of ~7 Å are characteristic of the [Fe^{II}Pd(CN)$_4$] grids in a

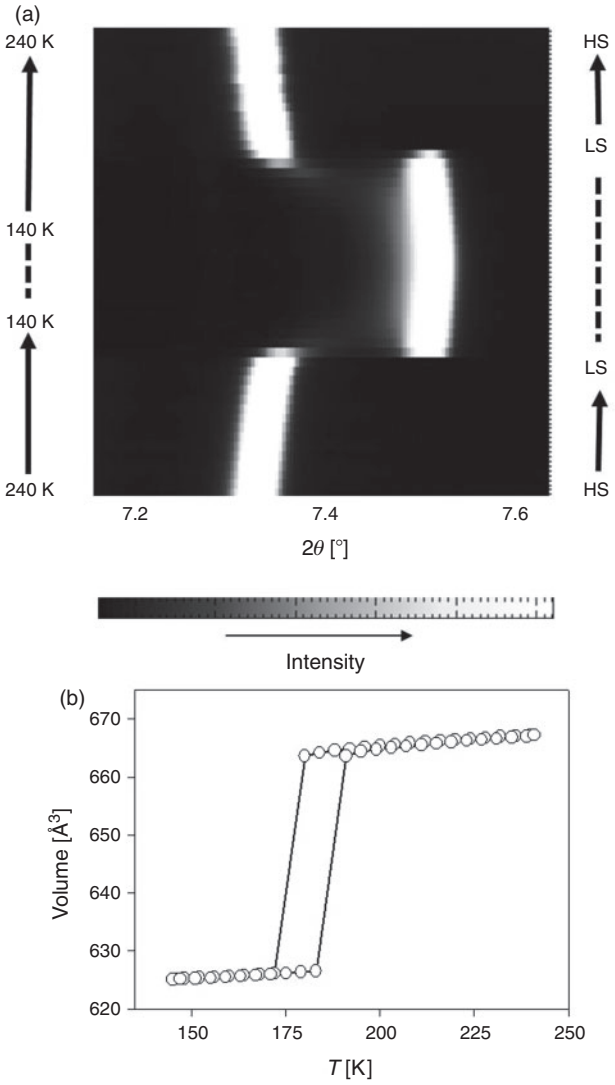

Fig. 4. Variable temperature synchrotron powder X-ray diffraction data of **A**: (a) single peak evolution over the range 7.2–7.6°, highlighting the abrupt shift in the Bragg reflection (0 −1 2) with temperature and (b) unit cell volume as a function of temperature plot determined by Le Bail refinement.

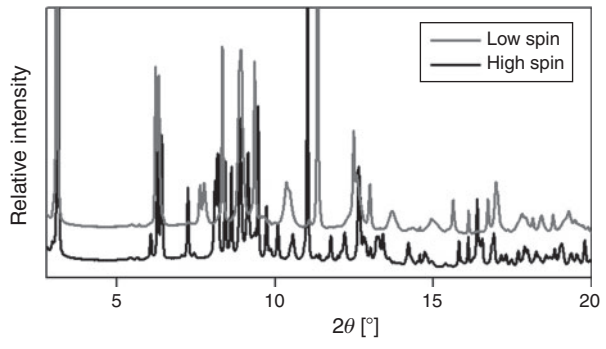

Fig. 5. Variable temperature powder X-ray diffraction data for **B** at 280 K (black) and 220 K (grey), representing the HS and LS states, respectively.

Hofmann-type material, whereby adjacent iron(II) sites are separated by this distance. The *c*-axis value relates to the interlayer separation of the $[Fe^{II}Pd(CN)_4]$ grids. The larger unit cell volume of **B** (~697 Å^3) compared with that of **A** (~667 Å^3) highlights the increased layer spacing owing to the perpendicular binding mode of the 4-PAP ligands. With cooling through the HS-to-LS spin transition, the peak positions reversibly vary, and some peak broadening and overlap is evident (see Fig. 5).

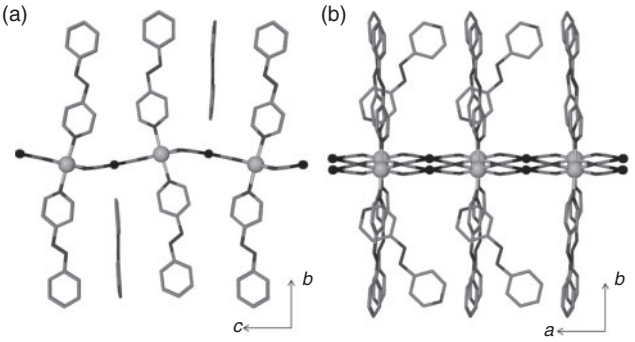

Fig. 6. Structural diagrams of **B·(4-PAP)** at 100 K showing a single 2D net, viewed along the (a) *a*-axis and (b) *c*-axis.

*Structural Analysis of $[Fe(4\text{-}PAP)_2Pd(CN)_4]\cdot(4\text{-}PAP)$ (**B·(4-PAP)**)*

Structural analysis of **B·(4-PAP)** at 100 K revealed monoclinic symmetry ($P2_1/c$) and an asymmetric unit consisting of one iron(II) site, one $[Pd(CN)_4]^{2-}$ group, two 4-PAP ligands, and a free 4-PAP ligand (Fig. 2b). As for **A**, the iron(II) site is in a distorted octahedral environment with four equatorially coordinated $[Pd(CN)_4]^{2-}$ metalloligands and two axially coordinated 4-PAP ligands. The overall structure is composed of undulating 2D $[Fe^{II}Pd(CN)_4]$ layers in the *ac*-plane separated by 4-PAP ligands, resulting in a 2D interdigitated Hofmann-type framework (Fig. 6). The undulating nature of the layer (octahedral tilt, Table 2) is similar to that observed for **A** in the HS state. However, in contrast to **A**, the 4-coordination mode of the 4-PAP ligands results in a more perpendicular arrangement of layers and ligands, although the combination of octahedral tilt and symmetry considerations results in alternating smaller and larger pockets of space along the *c*-direction (Fig. 6a). Adjacent 4-PAP ligands in the smaller pockets interact via weak N···C(H) interactions (Table 2). Free 4-PAP ligands reside within the larger pockets and participate in weak C(H)···π interactions with the bound 4-PAP ligands (Fig. 6). The 2D nets are close-packed, with a near-complete overlap of the interdigitated ligands and no notable void volume apart from that occupied by the free ligand.

The average Fe–N bond lengths ($<d_{Fe-N}>$, Table 2) at 100 K of ~2.1 Å are consistent with iron(II) sites in the HS state, indicating that the material is SCO-inactive <100 K. In assessing the structural aspects that may contribute to the stabilisation of the HS state, we note first that the Fe^{II} coordination environment generally appears conducive to conversion to the LS state (e.g. the octahedral distortion parameter and Fe–N≡C angles are comparable with that of **A** in the LS state). The free ligand in the pores may therefore play an important role through an internal pressure effect, inhibiting the volumetric contraction associated with the HS-to-LS transition. A similar internal pressure effect has been observed through the use of exchangeable molecular guests of varying sizes in related Hofmann phases.[42]

*Optical Reflectivity Measurements on **A** and **B***

Measurement of the visible spectrum of the sample as function of temperature, using diffuse reflectance, provides a convenient

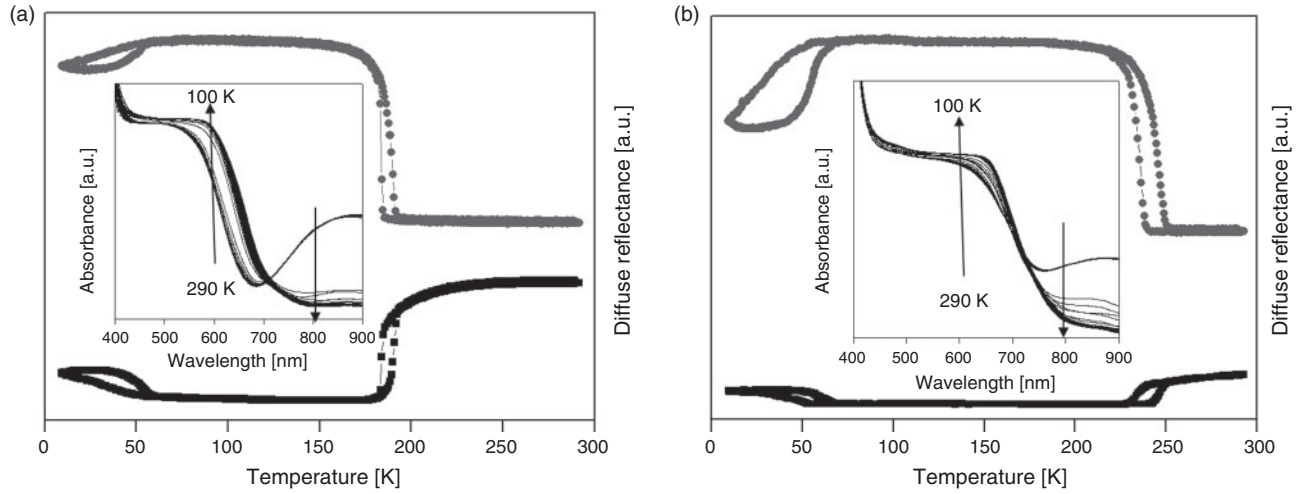

Fig. 7. Thermal dependence of the diffuse reflectance measured at 600 nm (black) and 860 nm (grey) for (a) **A** and (b) **B**, from 290 to 100 K for the thermal SCO and from 100 to 10 K for the LIESST effect. Insets show the thermal variation of the reflectance spectra of **A** and **B**.

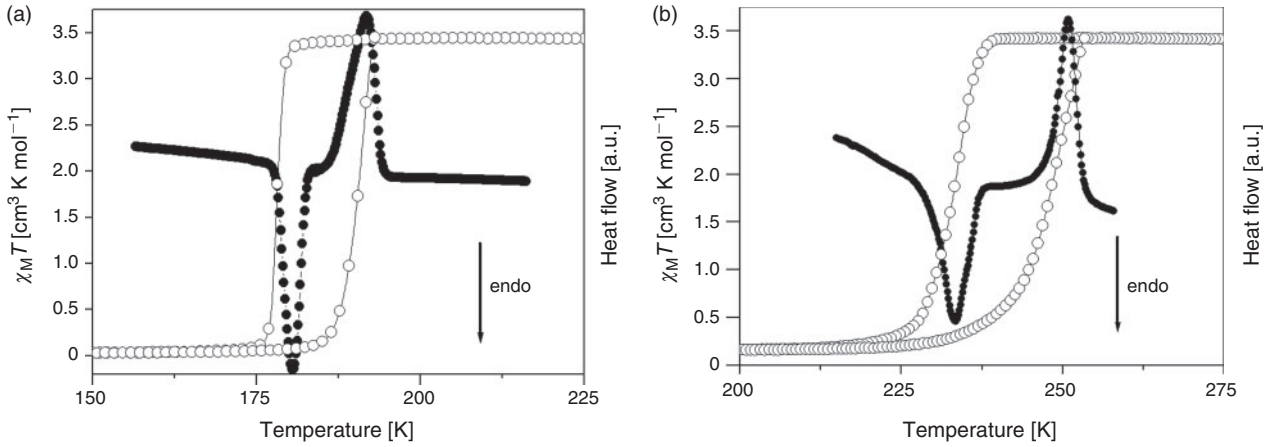

Fig. 8. Plots of $\chi_M T$ as a function of temperature (open markers) and associated DSC curves (closed markers) for (a) **A** and (b) **B**.

means to monitor thermal and light-induced SCO. The spectral changes for **A** and **B** observed upon cooling from 300 to 100 K are quite pronounced, especially between 600 and 900 nm, confirming the occurrence of a thermal SCO (insets in Fig. 7). Upon cooling, the band centred at 850 nm (which is characteristic of the d–d transition of the HS state) decreases sharply, and concomitantly, the bands around 400–600 nm (assigned to both d–d and metal-to-ligand (MLCT) transitions of the LS state) increase. These changes reflect the thermally induced HS-to-LS SCO transition that can be directly monitored by the thermal dependence of the reflectivity signals at 850 and 600 nm (Fig. 7). These latter curves indicate that the thermal SCO occurs with a hysteresis loop, with characteristic temperatures of 190 K ($T_{1/2}\uparrow$) and 183 K ($T_{1/2}\downarrow$) for **A**, and 245 K ($T_{1/2}\uparrow$) and 234 K ($T_{1/2}\downarrow$) for **B**. With further cooling from 80 to 10 K, a slight reverse trend in these bands is observed. This indicates that at the surface of the sample a small LS-to-HS photo-conversion occurs owing to the LIESST effect, whereby LS iron(II) sites are excited to a metastable HS state under irradiation, and the lifetime of the metastable photo-induced HS state at 10 K is sufficiently long to allow optical excitation by a halogen light source. A hysteresis in the heating and cooling below 100 K is observed, indicating optical bi-stability and the LITH (light-induced thermal hysteresis) effect.

*Magnetic Properties of **A** and **B***

Magnetic susceptibility data for **A** and **B** reveal abrupt and hysteretic one-step SCO transitions (Fig. 8). For **A**, upon cooling from room temperature, the $\chi_M T$ values remain constant at ~3.44 cm^3 mol^{-1} K, indicating the presence of iron(II) in the HS state until 180 K, where there is a rapid decline to 0.55 cm^3 mol^{-1} K, representing a near-complete spin state conversion of the iron(II) sites to LS. The heating curve shows the same one-step SCO behaviour with a hysteresis loop of 12 K ($T_{1/2}\downarrow$: 178 K $T_{1/2}\uparrow$: 190 K). The differential scanning calorimetry (DSC) curve of compound **A** shows two peaks attributed to the one-step hysteretic SCO, at around 180 K (endo) and 190 (exo) (Fig. 8a). For **B**, upon cooling from room temperature, the $\chi_M T$ values remain constant at ~3.34 cm^3 mol^{-1} K, indicating the presence of iron(II) in the HS state until 240 K, where there is a rapid decline to 0.15 cm^3 mol^{-1} K, representing a near-complete spin state conversion of the iron(II) sites to LS. The heating curve shows the same one-step SCO behaviour with a hysteresis loop of 15 K ($T_{1/2}\downarrow$: 235 K $T_{1/2}\uparrow$: 250 K). Different degrees of completeness of the HS-to-LS transition were observed between sample batches and are related to the amount of **B·(4-PAP)** in the sample, which was determined to be a non-SCO material (above 100 K) by single crystal analysis. The DSC

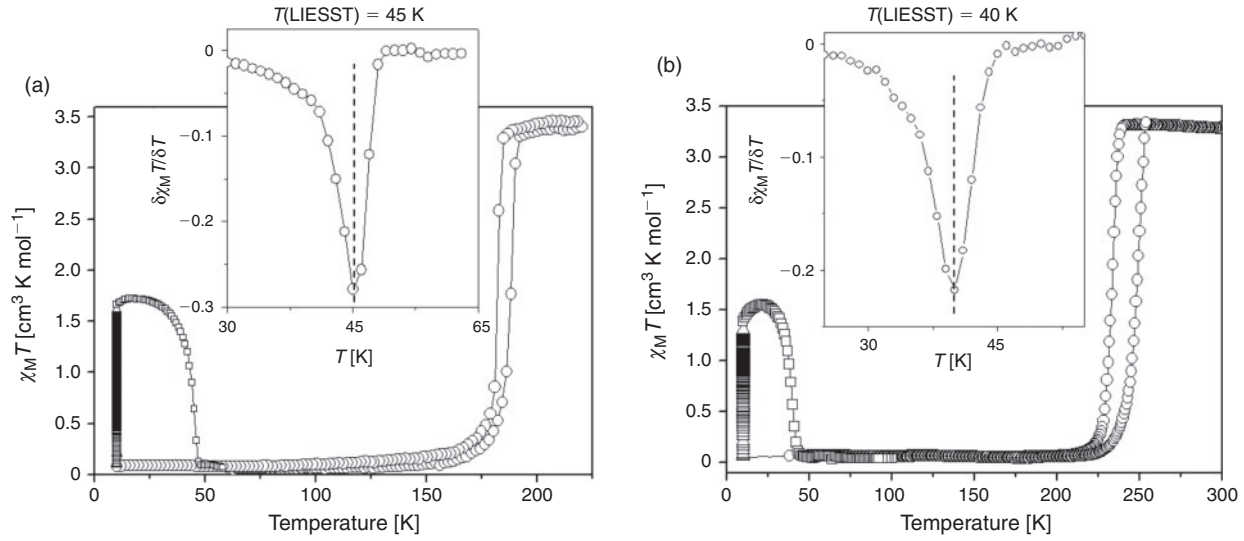

Fig. 9. Plots of $\chi_M T$ as a function of temperature for (a) **A** and (b) **B**, measured in the dark (circle markers), under irradiation at 10 K (triangle markers), and after irradiation in the dark (square markers). Insets show the associated derivative plots for **A** and **B**, and indicate the *T*(LIESST) values (minimum points).

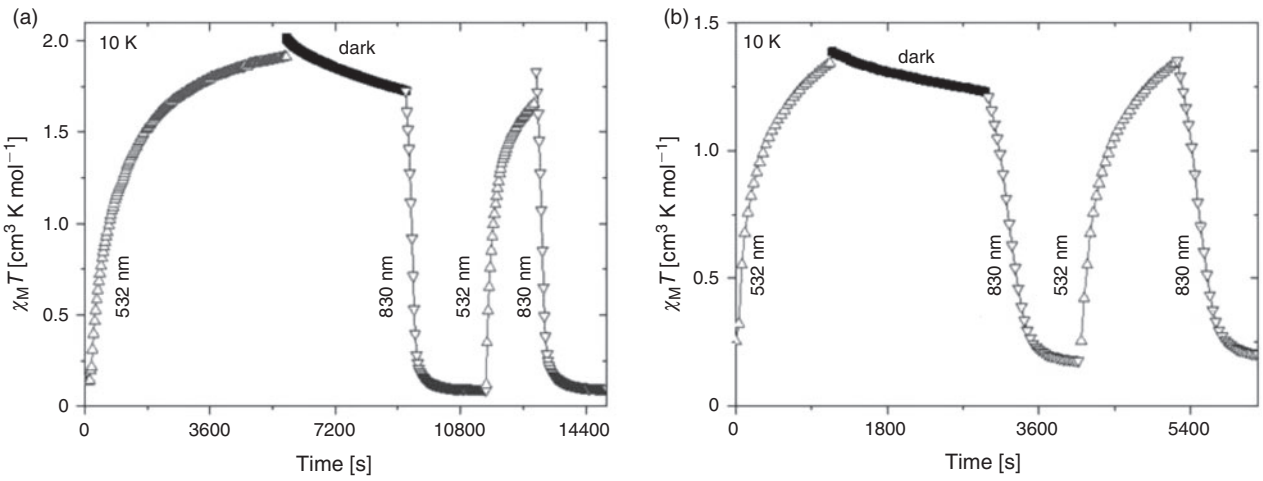

Fig. 10. Photo-reversibility of the metastable HS→ LS process in (a) **A** and (b) **B**; irradiation at 532 nm induces the LIESST effect (triangle markers), relaxation kinetics at 10 K in the dark (closed square markers), and irradiation at 830 nm induces the reverse-LIESST process (inverted triangle markers).

curve of compound **B** shows two peaks attributed to the one-step hysteretic SCO, at around 233 K (endo) and 250 (exo) (Fig. 8b).

Reflectivity measurements on **A** and **B** revealed the presence of photo-excitation signals at low temperatures upon irradiation. Subsequent detailed photo-magnetic studies on **A** and **B** were performed; using irradiation at 532 nm at 10 K, photo-excitation of the LS species to a metastable HS state was observed (Fig. 9). Upon irradiation, an increase in $\chi_M T$ was observed, reaching saturation at 1.74 cm^3 K mol^{-1} and 1.52 cm^3 K mol^{-1} for **A** and **B**, respectively (Fig. 9). This indicates a photo-excitation efficiency of around 50 %. The temperature at which the photo-induced trapped information is erased (when the temperature is increased from 10 K at a rate of 0.3 K min^{-1} inside a SQUID cavity),[11,12] *T*(LIESST) values are 45 and 40 K for **A** and **B**, respectively (Fig. 9, inset). The $T_{1/2}$ and *T*(LIESST) values of **A** and **B** were around the $T_0 = 100$ K value of the linear relationship established between the transition temperature ($T_{1/2}$) and *T*(LIESST) values ($T(\text{LIESST}) = T_0 - 0.3T_{1/2}$).[52] This line is associated mainly with monodentate ligands, and corresponds well with the binding mode of the 3- and 4- PAP ligands but not the Hofmann layer.

For **A** and **B**, the stability of the photo-induced HS state was assessed (after irradiation at 532 nm) by recording $\chi_M T$ values in the dark, and shows a slow decrease over 1 h (Fig. 10). The reverse-LIESST process (metastable HS→LS) was accelerated upon irradiation at 830 nm, whereby the LS state was completely recovered in less than 30 min. A cycling experiment of the 'metastable HS' and 'LS' states was subsequently carried out, and illustrated the occurrence of both LIESST (switch 'on') and reverse-LIESST (switch 'off') processes in these compounds (Fig. 10).

There is a clear difference in the thermal and photo-induced SCO behaviours between **A** and **B**, as reflected by the significant increase in the transition temperature of ~70 K for **B** and the lack of SCO in **B·(4-PAP)**. This result highlights that subtle packing and ligand field effects play a major role in the overall magnetic properties.[53] In assessing the increase in transition temperature of **A** and **B**, even in the absence of a direct structural

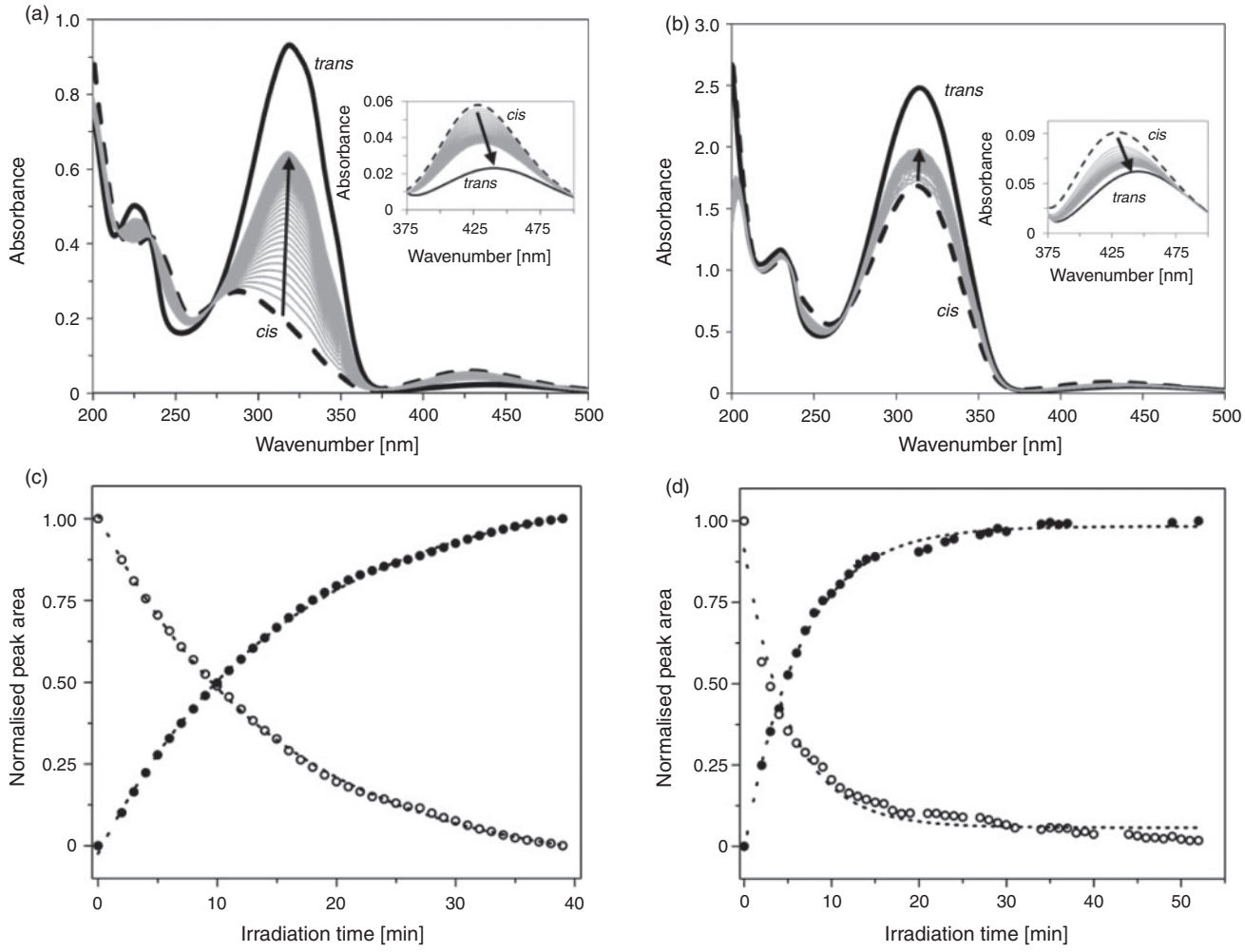

Fig. 11. UV–vis absorbance spectra showing excitation of (a) 3-PAP and (b) 4-PAP in ethanol/H_2O. The black dotted curves were generated at the start of the experiment and the black solid curved were obtained following exposure to UV irradiation (365 nm) for 60 min. The grey curves show the change of the spectra under ambient light over time. The inset plots show an expanded view of the n–π* band for 3-PAP and 4-PAP. The evolution of the n–π* (open circles) and π–π* (solid circles) bands indicates the relaxation of excited (c) 3-PAP and (d) 4-PAP. All curves were fitted with an exponential decay model (dotted lines).

comparison between the two materials, there are several possible origins of this behaviour that can be considered. First, binding of the 4-PAP ligand to the iron(II) sites to generate a perpendicular pillar would lead to a more efficient orbital overlap compared with that of the 3-PAP ligand which results in a diagonal ligand orientation. Secondly, in comparing the $[Fe^{II}Pd(CN)_4]$ layer spacing between the two materials, **A** is more compact than **B**, which in a related set of materials was suggested to allow for more efficient propagation of long-range elastic interactions.[54] Here, the opposite behaviour is observed, with **B** showing a larger layer spacing, indicating that there may be sufficient ligand–ligand interactions within the pore space to allow efficient propagation of SCO, irrespective of the distance between the SCO sites.

*UV–Visible Spectroscopy of **A** and **B***

The 3- and 4-PAP ligands contain an azo-benzene functional group that is known to undergo a *trans*-to-*cis* isomerisation upon absorption of UV light. The ground state of azo-benzene is the *trans*-conformation that shows a planar geometry. Upon absorption of UV light, the *cis*-state is induced, which exhibits a non-planar structural geometry. The reverse transition can be induced either by illumination with visible light or by thermal relaxation. Both isomers have distinct UV–vis spectra and thus, the conversion process and conformation can readily be distinguished. In particular, the *trans*-isomer exhibits a strong π–π* absorption band at ~340 nm and the *cis*-isomer an n–π* band at ~450 nm. In assessing the potential photo-activity of the 3- and 4-PAP ligands in **A** and **B**, the behaviour of the free ligands in solution (ethanol/water) was evaluated. Fig. 11a, b shows the UV–vis spectra recorded for 3-PAP and 4-PAP. Upon irradiation for 1 h with UV light (λ 365 nm), a pronounced increase and decrease in the relative intensity of the n–π* (320 nm) and π–π* (420 nm) bands was observed, respectively. This confirms that both the 3- and 4-PAP ligands undergo *trans*-to-*cis* isomerisation in the presence of UV light. In the absence of irradiation, the relaxation kinetics of the reverse process for both ligands indicate an exponential decay over a period of 60 min (Fig. 11c, d).

Solid state UV–vis measurements carried out on the free ligands and complexes **A** and **B** revealed the absence of a *trans*-to-*cis* ligand isomerisation and an overall increase in all bands, potentially because of sample heating. It is likely that the dense structural packing of both the free ligands and ligands within the

crystalline lattices of **A** and **B** inhibit the large geometry rearrangement necessary for the *trans*-to-*cis* isomerisation process to occur.[26,29,30]

Conclusion

A new family of 2D Hofmann-type materials have been synthesised using photoactive azo-benzene-type ligands (3-PAP and 4-PAP). Crystallographic, optical, and magnetic studies have probed the SCO properties of these materials, revealing abrupt and hysteretic spin transitions for the related materials $[Fe(L)_2Pd(CN)_4]$ (L = 3-PAP (**A**), 4-PAP (**B**)) and no spin transitions for $[Fe(4\text{-}PAP)_2Pd(CN)_4]\cdot(4\text{-}PAP)$ (**B·(4-PAP)**) containing free ligand within the pores. Furthermore, detailed photo-magnetic characterisation of the SCO phases revealed the presence of a LIESST behaviour with characteristic relaxation temperatures expected for monodentate organic ligand coordination. Photo-isomerisation properties of the free ligand in solution under UV light irradiation reveal a *trans*-to-*cis* conversion that is reversible in the absence of irradiation. However, in the solid state, both the free ligand and 2D framework materials (**A** and **B**) do not exhibit any significant conversion under the same conditions. In future work, we aim to apply the same strategy by incorporating longer azo-type ligands or azo-group covalently attached to the ligand into Hofmann-type materials to promote a more sterically favourable environment within the cavities to promote the *trans*-to-*cis* conversion.

Experimental

General

All reagents were commercially available and used as received (iron(II) perchlorate was handled carefully and in small amounts to avoid any potential explosions).

Ligand Synthesis

Both ligands were synthesised following the same synthesis procedure previously reported for **4-PAP**.[55]

3-Phenylazo-pyridine (3-PAP) and 4-Phenylazo-pyridine (4-PAP)

3- or 4-Aminopyridine (2.00 g, 21.2 mmol) and aqueous tetramethylammonium hydroxide solution (25 mL, 60 wt.-%) were dissolved in pyridine (25 mL). To this solution, nitrosobenzene (3.00 g, 28.0 mmol) in pyridine (50 mL) was added over 60 min at 80°C. The solution was then allowed to cool to room temperature, and extracted three times with toluene (50 mL). The extract was then washed with NaCl and dried with Na_2SO_4. The remaining organic solvent was removed under vacuum and the crude product separated and purified by column chromatography (**3-PAP**, 2 : 1 mixture of cyclohexane/ethyl acetate; **4-PAP**, 8 : 1 cyclohexane/ethyl acetate with 5 % triethylamine). A deep red solid resulted (3-PAP: 3.07 g, 79 %; 4-PAP: 2.77 g, 71 %). **3-PAP**: ν_{max} (KBr/cm^{-1} 3065 (m), 1958 (w), 1899 (w), 1586 (m), 1568 (m), 1479 (m), 1460 (m), 1441 (m), 1417 (m), 1320 (w), 1301 (w), 1247 (w), 1228 (w), 1191 (m), 1149 (w), 1114 (w), 1093 (m), 1071 (m), 1022 (m), 1000 (w), 964 (m), 928 (m), 816 (s), 766 (s), 703 (s), 689 (s), 618 (w), 553 (m), 537 (m), 524 (m), 473 (m). δ_H ([D4]MeOD, 200 MHz) 9.25 (1H, s), 8.78 (1H, d, $^3J_{HH}$ 5), 8.20 (1H, d, $^3J_{HH}$ 8), 7.99 (2H, t, $^3J_{HH}$ 2), 7.60 (3H, d, $^3J_{HH}$ 6), 7.51 (1H, dd, $^3J_{HH}$ 5, $^3J_{HH}$ 11). *m*/*z* (ESI) 184.00 (M+H). Anal. Calc. for $C_{11}N_3H_9$: C 72.11, N 22.94, H 4.95. Found: C 72.13, N 22.91, H 4.75 %. **4-PAP**: δ_H ([D4]MeOD, 200 MHz) 8.90 (2H, d, $^3J_{HH}$ 9), 8.02 (2H, d, $^3J_{HH}$ 10), 7.77 (2H, d, $^3J_{HH}$ 9), 7.61 (3H, d, $^3J_{HH}$ 7).[55]

Complex Synthesis

$[Fe(3\text{-}PAP)_2Pd(CN)_4]$ (**A**)

Single crystals were prepared by vial-in-vial slow diffusion method, whereby 3-PAP (27 mg, 0.12 mmol) and $K[Pd(CN)_4]$ (17 mg, 0.06 mmol) were placed at the base of a small vial and $Fe(ClO_4)_2\cdot 6H_2O$ (15 mg, 0.06 mmol) was placed at the base of a large vial. The small vial was placed inside the large vial and both were carefully filled with a 50 : 50 ethanol/water mixture. The components were allowed to diffuse over a period of 2 weeks after which, well-formed red square plate-shaped crystals were formed. ν_{max} (KBr/cm^{-1} 2172 (s), 1605 (w), 1587 (w), 1574 (w), 1488 (w), 1461 (w), 1443 (w), 1427 (w), 1384 (w), 1322 (w), 1301 (w), 1195 (w), 1158 (w), 1144 (w), 1116 (w), 1096 (w), 1069 (w), 1044 (w), 1029 (w), 1000 (w), 928 (w), 837 (w), 812 (m), 767 (m), 694 (m), 686 (s), 640 (w), 614 (w), 556 (w), 539 (w), 528 (w), 500 (w), 483 (w), 423 (s). Anal. Calc. for $C_{26}N_{10}H_{18}$: C 49.35, N 22.14, H 2.87. Found: C 48.10, N 21.53, H 2.63 %.

$[Fe(4\text{-}PAP)_2Pd(CN)_4]$ (**B**) and $[Fe(4\text{-}PAP)_2Pd(CN)_4]\cdot 1/2(4\text{-}PAP)$ (**B·(4-PAP)**)

A mixture of single crystals and polycrystalline powder containing both **B** and **B·(4-PAP)** were prepared by vial-in-vial slow diffusion method, whereby 4-PAP (27 mg, 0.12 mmol) and $K[Pd(CN)_4]$ (17 mg, 0.06 mmol) were placed at the base of a small vial and $Fe(ClO_4)_2\cdot 6H_2O$ (15 mg, 0.06 mmol) was placed at the base of a large vial. The small vial was placed inside the large vial and both were carefully filled with a 50 : 50 ethanol/water mixture. The components were allowed to diffuse over a period of 2 weeks after which, well-formed red square plate-shaped crystals of **B·(4-PAP)** and red polycrystalline clumps of **B** were formed. ν_{max} (KBr/cm^{-1} 2171 (s), 1605 (m), 1486 (w), 1397 (w), 1385 (w), 1316 (w), 1267 (w), 1232 (w), 1208 (w), 1146 (w), 1121 (w), 1091 (w), 1030 (w), 1016 (w), 1006 (w), 954 (w), 905 (w), 836 (m), 798 (w), 768 (w), 681 (m), 628 (w), 556 (w), 541 (w), 525 (w), 421 (m), 408 (w). Anal. Calc. for $C_{26}N_{10}H_{18}$: C 49.35, N 22.14, H 2.87. Found: C 48.66, N 21.19, H 2.68 %.

Thermogravimetric Analysis (TGA)

Analyses were carried out on a TA Instruments Hi-Res TGA 2950 Thermogravimetric Analyzer. The samples were heated between room temperature and 873 K at 1 K min^{-1}. The atmosphere was controlled with a dry nitrogen supply (0.1 L min^{-1}) and around 5 mg sample was used for each measurement (see Supplementary Material).

Differential Scanning Calorimetry (DSC)

Calorimetric measurements were performed using a differential scanning calorimeter (Mettler Toledo DSC 823e). The measurements were carried out using ~2 mg of powdered sample sealed in 40 µL aluminium pans with a mechanical crimp (an empty pan was used as a reference). The sample holder was kept in a dry box under a flow of dry nitrogen gas (50 mL min^{-1}) to avoid water condensation. The DSC instrument was liquid-nitrogen cooled.

Single Crystal X-Ray Diffraction

Single crystal diffraction data were collected at 150 and 220 K on crystals of **A**, and at 100 K on **B·(4-PAP)**. Data for **A** were collected using a Bruker APEX diffractometer equipped with a rotating anode (λ 0.7017 Å) and an Oxford Cryosystems nitrogen gas open flow cryostat. The crystals were twinned and processed within the *APEX* software suite and empirical absorption corrections were carried out within *TWINABS*.[56,57] Data for **B·(4-PAP)** were collected on an Agilent SuperNova Dual Source diffractometer employing a $Cu_{K\alpha}$ radiation source (λ 1.5418 Å). Data integration and reduction were performed using *CrysAlisPro*.[58]

Structural solution analysis for all materials was completed within *SHELXS-97* and refined using *SHELXL-97* within the *X-SEED* user interface.[59,60] All atoms were refined anisotropically and hydrogen atoms were fixed using the riding model. A summary of the crystallographic and refinement details are presented in Table 1 and the relevant structural parameters are listed in Table 2. The CCDC reference numbers are 993492–993494.

Variable Temperature Synchrotron Powder Diffraction

Polycrystalline samples of **A** and **B** were ground as a slurry and loaded into a quartz capillary (0.7 mm diameter) that was sealed to prevent solvent loss. The X-rays (17.03 keV, 0.72808 Å) available at the 17-BM beamline at the Advanced Photon Source at Argonne National Laboratory were used in combination with a Perkin–Elmer area detector with a carbon window to record diffraction patterns. The sample temperature was controlled using an Oxford Cryosystems open flow cryostat, and the data were collected at intervals of 20 s upon continuous heat increase over the range of 300–100 K at 120 K h^{-1}. This corresponds to the collection of diffraction images at 2 K intervals. The raw images were processed using *Fit-2D*.[61,62] Lanthanium hexaboride (LaB_6) was used as a standard. Le Bail analyses of the diffraction data were performed within *TOPAS*.[51]

Magnetic Susceptibility Measurements

Data for magnetic susceptibility measurements were collected on a Quantum Design Versalab Measurement System with a Vibrating Sample Magnetometer (VSM) attachment. Measurements were taken continuously under an applied field of 0.3 T over the temperature range 50–300 K at a heating ramp of either 2 or 4 K min^{-1} as indicated. Several cycles of each cooling and heating experiment were carried out to check for consistency. Several samples of **B** (containing a mixture of different ratios of **B** and **B·(4-PAP)**) were analysed to assess the fraction of each product present, as evidenced by the degree of HS residual fraction at low temperatures (Fig. S4).

The photo-magnetic measurements were performed on **A** and **B** using a set of photodiodes coupled via an optical fibre to the cavity of a MPMS-5S Quantum Design SQUID magnetometer operating at 2 T. Samples were prepared as a thin layer (~0.1 mg) to promote full penetration of the irradiated light. The sample mass was obtained by comparison with the thermal spin transition curve measured on a larger, accurately weighed polycrystalline sample.[11,52,63,64] The sample was first slowly cooled to 10 K, ensuring that potential trapping of HS species at low temperatures did not occur. Irradiation to photo-saturation was conducted at 532 nm and the power of the sample surface was adjusted to prevent heating of the sample. Once photo-saturation was reached, irradiation was ceased and the temperature was increased to 100 K at a rate of 0.3 K min^{-1}. Magnetisation data were recorded every 1 K to determine the T(LIESST) value which obtained by the $\delta\chi_M T/\delta T$–T curve. The T(LIESST) value describes the limiting temperature above which the light-induced magnetic high-spin information is erased in a SQUID cavity.[11,52,63,64] The magnetism was also measured in the absence of irradiation over the temperature range of 10–300 K to monitor the thermal spin transition and to obtain a low-temperature baseline. In addition, reverse LIESST measurements were performed by first attaining complete photo-saturation by irradiation of the sample at 10 K, then irradiating with red light.

Optical Reflectivity

Optical reflectivity measurements were carried out on **A** and **B** using a custom-built reflectivity setup coupled with a CVI spectrometer. Reflectivity spectra within the range of 400–900 nm and the temperature dependence of the signal at selected wavelengths (600 and 860 nm) were simultaneously recorded. The source of white light consisted of a halogen lamp emitting between 400 and 900 nm. The analyses were performed directly at the surface of the thin layers of the crystalline samples without any dispersion in a matrix.

Optical Spectroscopy Measurements

UV–vis spectra in solution (ethanol/H_2O) were recorded on a CARY 500 UV/Vis/Near IR spectrometer at room temperature. Quarts cells (path length: 10 mm) were used for the measurements. A baseline was measured using a sample and a reference cell filled with pure solvent before measurements. The *trans–cis* isomerisation was achieved by irradiating the sample with a 365-nm ultraviolet hand lamp (ENF-240C/FE, Spectroline) for 1 h. Relaxation to the *trans*-ground state was achieved by exposure to ambient light.

Supplementary Material

Thermogravimetric analysis data, synchrotron-based powder X-ray diffraction data, single crystal details and magnetic susceptibility data are available on the Journal's website.

Acknowledgements

This work was supported by a Fellowship and a Discovery Project funding from the Australian Research Council. Access and use of the facilities of the Advanced Photon Source (APS) was supported by the USA Department of Energy, Office of Science, Office of Basic Energy Sciences (Contract No. DE-AC02–06CH11357). The authors thank Dr Gregory J. Halder for beamline support. Travel to the APS was funded by the International Synchrotron Access Program (ISAP) managed by the Australian Synchrotron and funded by the Australian Government. The authors also thank the Aquitaine Region for supporting the development of the international platform of photo-magnetism.

References

[1] O. Kahn, C. J. Martinez, *Science* **1998**, *279*, 44. doi:10.1126/SCIENCE.279.5347.44

[2] J.-F. Létard, P. Guionneau, L. Goux-Capes, *Top. Curr. Chem.* **2004**, *235*, 221. doi:10.1007/B95429

[3] M. A. Halcrow, *Spin-Crossover Materials: Properties and Applications* **2013** (John Wiley & Sons, Ltd: Chichester).

[4] P. Gütlich, A. B. Gaspar, Y. Garcia, *Beilstein J. Org. Chem.* **2013**, *9*, 342. doi:10.3762/BJOC.9.39

[5] M. Natali, S. Giordani, *Chem. Soc. Rev.* **2012**, *41*, 4010. doi:10.1039/C2CS35015G

[6] P. Gütlich, H. A. Goodwin, *Top. Curr. Chem.* **2004**, *233*, 1. doi:10.1007/B13527

[7] P. Gütlich, A. Hauser, H. Spiering, *Angew. Chem. Int. Ed.* **1994**, *33*, 2024. doi:10.1002/ANIE.199420241

[8] A. Bleuzen, V. Marvaud, C. Mathoniere, B. Sieklucka, M. Verdaguer, *Inorg. Chem.* **2009**, *48*, 3453. doi:10.1021/IC802007G

[9] S. Decurtins, P. Gütlich, C. P. Köhler, H. Spiering, A. Hauser, *Chem. Phys. Lett.* **1984**, *105*, 1. doi:10.1016/0009-2614(84)80403-0

[10] A. Hauser, *Chem. Phys. Lett.* **1986**, *124*, 543. doi:10.1016/0009-2614(86)85073-4

[11] J.-F. Létard, P. Guionneau, L. Rabardel, J. A. K. Howard, A. E. Goeta, D. Chasseau, O. Kahn, *Inorg. Chem.* **1998**, *37*, 4432. doi:10.1021/IC980107B

[12] J.-F. Létard, L. Capes, G. Chastanet, N. Moliner, S. Létard, J. A. Real, O. Kahn, *Chem. Phys. Lett.* **1999**, *313*, 115. doi:10.1016/S0009-2614(99)01036-2

[13] S. Marcén, L. Lecren, L. Capes, H. A. Goodwin, J.-F. Létard, *Chem. Phys. Lett.* **2002**, *358*, 87. doi:10.1016/S0009-2614(02)00590-0

[14] F. Varret, K. Boukheddaden, G. Chastanet, N. Paradis, J.-F. Létard, *Eur. J. Inorg. Chem.* **2013**, 763. doi:10.1002/EJIC.201200863

[15] E. Buhks, G. Navon, M. Bixon, J. Jortner, *J. Am. Chem. Soc.* **1980**, *102*, 2918. doi:10.1021/JA00529A009

[16] A. Hauser, *Coord. Chem. Rev.* **1991**, *111*, 275. doi:10.1016/0010-8545(91)84034-3

[17] S. Bonhommeau, G. Molnár, A. Galet, A. Zwick, J. A. Real, J. J. McGarvey, A. Bousseksou, *Angew. Chem. Int. Ed.* **2005**, *44*, 4069. doi:10.1002/ANIE.200500717

[18] C. Roux, J. Zarembowitch, B. Gallois, T. Granier, R. Claude, *Inorg. Chem.* **1994**, *33*, 2273. doi:10.1021/IC00088A033

[19] K. Sénéchal-David, N. Zaman, M. Walko, E. Halza, E. Rivière, R. Guillot, B. L. Feringa, M.-L. Boillot, *Dalton Trans.* **2008**, 1932. doi:10.1039/B715017B

[20] M.-L. Boillot, S. Pillet, E. Rivière, N. Claiser, C. Lecomte, *Inorg. Chem.* **2009**, *48*, 4729. doi:10.1021/IC802319C

[21] Y. Hasegawa, S. Kume, H. Nishihara, *Dalton Trans.* **2009**, 280. doi:10.1039/B817196N

[22] A. Tissot, M.-L. Boillot, S. Pillet, E. Codjovi, K. Boukheddaden, L. M. L. Daku, *J. Phys. Chem. C* **2010**, *114*, 21715. doi:10.1021/JP106583F

[23] M.-L. Boillot, S. Chantraine, J. Zarembowitch, J.-Y. Lallemand, J. Prunet, *New J. Chem.* **1999**, *23*, 179. doi:10.1039/A809504C

[24] S. Hirose, S. Hayami, Y. Maeda, *Bull. Chem. Soc. Jpn.* **2000**, *73*, 2059. doi:10.1246/BCSJ.73.2059

[25] Y. Hasegawa, S. Kume, H. Nishihara, *Dalton Trans.* **2009**, 280. doi:10.1039/B817196N

[26] A. Modrow, D. Zargarani, R. Herges, N. Stock, *Dalton Trans.* **2011**, *40*, 4217. doi:10.1039/C0DT01629B

[27] J. Park, D. Yuan, K. T. Pham, J.-R. Li, A. Yakovenko, H.-C. Zhou, *J. Am. Chem. Soc.* **2012**, *134*, 99. doi:10.1021/JA209197F

[28] L. Heinke, M. Cakici, M. Dommaschk, S. Grosjean, R. Herges, S. Bräse, C. Wöll, *ACS Nano* **2014**, *8*, 1463. doi:10.1021/NN405469G

[29] D. Hermann, H. Emerich, R. Lepski, D. Schaniel, U. Ruschewitz, *Inorg. Chem.* **2013**, *52*, 2744. doi:10.1021/IC302856B

[30] J. W. Brown, B. L. Henderson, M. D. Kiesz, A. C. Whalley, W. Morris, S. Grunder, H. Deng, H. Furukawa, J. I. Zink, J. F. Stoddart, O. M. Yaghi, *Chem. Sci.* **2013**, *4*, 2858.

[31] J. A. Real, E. Andres, M. C. Muñoz, M. Julve, T. Granier, A. Bousseksou, F. Varret, *Science* **1995**, *268*, 265. doi:10.1126/SCIENCE.268.5208.265

[32] G. J. Halder, C. J. Kepert, B. Moubaraki, K. S. Murray, J. D. Cashion, *Science* **2002**, *298*, 1762. doi:10.1126/SCIENCE.1075948

[33] S. M. Neville, B. Moubaraki, K. S. Murray, C. J. Kepert, *Angew. Chem. Int. Ed.* **2007**, *46*, 2059. doi:10.1002/ANIE.200603977

[34] G. J. Halder, K. W. Chapman, S. M. Neville, B. Moubaraki, K. S. Murray, J.-F. Létard, C. J. Kepert, *J. Am. Chem. Soc.* **2008**, *130*, 17552. doi:10.1021/JA8068038

[35] S. M. Neville, G. J. Halder, K. W. Chapman, M. B. Duriska, P. D. Southon, J. D. Cashion, J.-F. Létard, B. Moubaraki, K. S. Murray, C. J. Kepert, *J. Am. Chem. Soc.* **2008**, *130*, 2869. doi:10.1021/JA077958F

[36] S. M. Neville, G. J. Halder, K. W. Chapman, M. B. Duriska, B. Moubaraki, K. S. Murray, C. J. Kepert, *J. Am. Chem. Soc.* **2009**, *131*, 12106. doi:10.1021/JA905360G

[37] T. Kitazawa, Y. Gomi, M. Takahashi, M. Takeda, M. Enomoto, A. Miyazaki, *J. Mater. Chem.* **1996**, *6*, 119. doi:10.1039/JM9960600119

[38] V. Niel, J. M. Martinez-Agudo, M. C. Munoz, A. B. Gaspar, J. A. Real, *Inorg. Chem.* **2001**, *40*, 3838. doi:10.1021/IC010259Y

[39] V. Martinez, Z. A. Castillo, M. C. Munoz, A. B. Gaspar, C. Etrillard, J.-F. Letard, S. A. Terekhov, G. V. Bukin, G. Levchenko, J. A. Real, *Eur. J. Inorg. Chem.* **2013**, *2013*, 813. doi:10.1002/EJIC.201201097

[40] G. Agustí, A. B. Gaspar, M. C. Mñnoz, P. G. Lacroix, J. A. Real, *Aust. J. Chem.* **2009**, *62*, 1155. doi:10.1071/CH09100

[41] V. Martínez, A. B. Gaspar, M. C. Muñoz, G. V. Bukin, G. Levchenko, J. A. Real, *Chem. Eur. J.* **2009**, *15*, 10960. doi:10.1002/CHEM.200901391

[42] P. D. Southon, L. Liu, E. A. Fellows, D. J. Price, G. J. Halder, K. W. Chapman, B. Moubaraki, K. S. Murray, J.-F. Létard, C. J. Kepert, *J. Am. Chem. Soc.* **2009**, *131*, 10998. doi:10.1021/JA902187D

[43] R. Ohtani, K. Yoneda, S. Furukawa, N. Horike, S. Kitagawa, A. B. Gaspar, M. C. Muñoz, J. A. Real, M. Ohba, *J. Am. Chem. Soc.* **2011**, *133*, 8600. doi:10.1021/JA111674C

[44] H. Shepherd, C. Bartual-Murgui, G. Molnàr, J. A. Real, M. C. Muñoz, L. Salmon, A. Bousseksou, *New J. Chem.* **2011**, *35*, 1205. doi:10.1039/C0NJ00845A

[45] K. Takahashi, Y. Hasegawa, R. Sakamoto, M. Nishikawa, S. Kume, E. Nishibori, H. Nishihara, *Inorg. Chem.* **2012**, *51*, 5188. doi:10.1021/IC300030B

[46] N. Yanai, T. Uemura, M. Inoue, R. Matsuda, T. Fukushima, M. Tsujimoto, S. K. Isoda, *J. Am. Chem. Soc.* **2012**, *134*, 4501. doi:10.1021/JA2115713

[47] K. Uemura, R. Matsuda, S. Kitagawa, *J. Solid State Chem.* **2005**, *178*, 2420. doi:10.1016/J.JSSC.2005.05.036

[48] C. M. Grunert, S. Reiman, H. Spiering, J. A. Kitchen, S. Brooker, P. Gütlich, *Angew. Chem. Int. Ed.* **2008**, *47*, 2997. doi:10.1002/ANIE.200705778

[49] S. G. Telfer, B. Bocquet, A. F. Williams, *Inorg. Chem.* **2001**, *40*, 4818. doi:10.1021/IC015521H

[50] Y. M. Klein, N. F. Sciortino, F. Ragon, C. E. Housecroft, C. J. Kepert, S. M. Neville, *Chem. Commun.* **2014**, *50*, 3838. doi:10.1039/C4CC01079E

[51] Bruker ASX, *TOPAS ver. 4.2* **2009**.

[52] J.-F. Létard, *J. Mater. Chem.* **2006**, *16*, 2550. doi:10.1039/B603473J

[53] M. Halcrow, *Chem. Soc. Rev.* **2011**, *40*, 4119. doi:10.1039/C1CS15046D

[54] R. Othani, M. Arai, H. Ohba, A. Hori, M. Takata, S. Kitagawa, M. Ohba, *Eur. J. Inorg. Chem.* **2013**, 738. doi:10.1002/EJIC.201201204

[55] N. R. Ayyangar, S. N. Naik, K. V. Srinivasan, *Tetrahedron Lett.* **1989**, *30*, 7253. doi:10.1016/S0040-4039(01)93951-6

[56] G. M. Sheldrick, *TWINABS* **1996** (University of Gottingen: Gottingen).

[57] *APEX II* Software Package **2005** (Bruker AXS Inc.: Madison, WI).

[58] *CrysAlisPro* (Agilent Technologies XRD Products: Yarnton, Oxfordshire).

[59] G. M. Sheldrick, *SHELX97 Programs for Crystal Structure Analysis* **1998** (University of Göttingen: Göttingen).

[60] L. J. Barbour, *J. Supramol. Chem.* **2001**, *1*, 189. doi:10.1016/S1472-7862(02)00030-8

[61] A. P. Hammersley, S. O. Svensson, M. Hanfland, A. N. Fitch, D. Hausermann, *High Pressure Res.* **1996**, *14*, 235. doi:10.1080/08957959608201408

[62] A. P. Hammersley, *ESRF Internal Report*. ESRF97HA02T **1997** (ESRF: Grenoble).

[63] A. Hauser, *Top. Curr. Chem.* **2004**, *234*, 155. doi:10.1007/B95416

[64] J. F. Létard, P. Guionneau, O. Nguyen, J. S. Costa, S. Marcén, G. Chastanet, M. Marchivie, L. Goux-Capes, *Chem. Eur. J.* **2005**, *11*, 4582. doi:10.1002/CHEM.200500112